Low-index nanopatterned barrier for hybrid oxide-free III-V silicon conductive bonding

Kristelle Bougot-Robin, Anne Talneau, Henri Benisty

Low-index nanopatterned barrier for hybrid oxide-free III-V silicon conductive bonding

Kristelle Bougot-Robin,[1,3] Anne Talneau,[2] and Henri Benisty[1,*]

[1]*Laboratoire Charles Fabry, UMR 8501, Institut d'Optique, CNRS, Université Paris-Sud 11, 2 Avenue Augustin Fresnel, 91127 Palaiseau, France*

[2]*Laboratoire de Photonique et de Nanostructures, CNRS-UPR20, Route de Nozay, 91460 Marcoussis, France*

[3]*Currently at Imperial College, London, UK*

[*]*henri.benisty@institutoptique.fr*

Abstract: Oxide-free bonding of a III-V active stack emitting at 1300-1600 nm to a silicon-on-insulator wafer offers the capability to electrically inject lasers from the silicon side. However, a typical 500-nm-thick silicon layer notably attracts the fundamental guided mode of the silicon + III-V stack, a detrimental feature compared to established III-V Separate-Confinement Heterostructure (SCH) stacks. We experimentally probe with photoluminescence as an internal light source the guiding behavior for oxide-free bonding to a nanopatterned silicon wafer that acts as a low-index barrier. We use a sub-wavelength square array of small holes as an effective "low-index silicon" medium. It is weakly modulated along one dimension (superperiodic array) to outcouple the resulting guided modes to free space, where we use an angle-resolved spectroscopy study. Analysis of experimental branches confirms the capability to operate with a fundamental mode well localized in the III-V heterostructures.

References and links

1. G. Roelkens, L. Liu, D. Liang, R. Jones, A. Fang, B. Koch, and J. Bowers, "III-V/silicon photonics for on-chip and inter-chip optical interconnects," Laser Photonics Rev. **4**(6), 751–779 (2010).
2. J. K. Doylend and A. P. Knights, "The evolution of silicon photonics as an enabling technology for optical interconnection," Laser & Photonics Reviews **6**(4), 504–525 (2012).
3. S. Keyvaninia, S. Verstuyft, S. F. Lelarge, G. H. Duan, S. Messaoudene, J. M. Fedeli, E. J. Geluk, T. D. Vries, B. Smalbrugge, J. Bolk, M. K. Smit, D. V. Thourhout, and G. Roelkens, "Heterogeneously integrated III-V/Si single mode lasers based on a MMI-ring configuration and triplet-ring reflectors," in SPIE Microtechnologies, 87670N, International Society for Optics and Photonics (2013).
4. I. Bakish, V. Artel, T. Ilovitsh, M. Shubely, Y. Ben-Ezra, A. Zadok, and C. N. Sukenik, "Self-assembled monolayer assisted bonding of Si and InP," Opt. Mater. Express **2**(8), 1141–1148 (2012).
5. K. Tanabe, K. Watanabe, and Y. Arakawa, "III-V/Si hybrid photonic devices by direct fusion bonding," Sci Rep **2**, 349 (2012).
6. K. Tanabe, K. Watanabe, and Y. Arakawa, "1.3 μm InAs/GaAs quantum dot lasers on Si rib structures with current injection across direct-bonded GaAs/Si heterointerfaces," Opt. Express **20**(26), B315–B321 (2012).
7. A. Talneau, C. Roblin, A. Itawi, O. Mauguin, L. Largeau, G. S. Beaudoin, I. G. Patriarche, C. Pang, and H. Benisty, "Atomic-plane-thick reconstruction across the interface during heteroepitaxial bonding of InP-clad quantum wells on Silicon," Appl. Phys. Lett. **102**(21), 212101 (2013).
8. K. Pantzas, A. Itawi, L. Couraud, J. C. Esnault, and E. Le Bourhis, "Electrical transport across the heterointerface of InP membranes bonded oxide-free on Si", paper TuD2–3, 26th International Conference on InP and Related Materials (IPRM 2014), Montpellier, May 11–15th, 2014.
9. J. H. Schmid, P. Cheben, P. J. Bock, R. Halir, J. Lapointe, S. Janz, A. Delâge, A. Densmore, J. Fedeli, T. J. Hall, B. Lamontagne, R. Ma, I. Molina-Fernandez, and D.-X. Xu, "Refractive index engineering with subwavelength gratings in silicon microphotonic waveguides," IEEE Photonics J. **3**(3), 597–607 (2011).
10. A. Itawi, K. Pantzas, I. Sagnes, G. Patriarche, and A. Talneau, "Void-free direct bonding of InP to Si: Advantages of low H-content and ozone activation," J. Vac. Sci. Technol. B **32**(2), 021201 (2014).

11. C. Pang, H. Benisty, B. Mondher, A. Talneau, and X. Pommarede, "Oxide-free InP-on-Silicon-on-Insulator nanopatterned waveguides: propagation losses assessment through end-fire and internal probe measurements," J. Lightwave Technol. **32**(6), 1048–1053 (2014).
12. C. Pang and H. Benisty, "Nanostructured silicon geometries for directly bonded hybrid III–V-silicon active devices," Photonics and Nanostructures-Fundamentals and Applications **11**(2), 145–156 (2013).
13. H. Benisty, J. Danglot, A. Talneau, S. Enoch, J. M. Pottage, and A. David, "Investigation of Extracting Photonic Crystal Lattices for Guided Modes of GaAs-Based Heterostructures," IEEE J. Quantum Electron. **44**(8), 777–789 (2008).
14. M. J. Mondry, D. I. Babic, J. E. Bowers, and L. A. Coldren, "Refractive Indexes of (Al, Ga, I n)As Epilayers on InP for Optoelectronic Applications," IEEE Photon. Technol. Lett. **4**(6), 627–630 (1992).
15. S. Olivier, M. Rattier, H. Benisty, C. J. M. Smith, R. M. De La Rue, T. F. Krauss, U. Oesterle, R. Houdré, and C. Weisbuch, "Mini stopbands of a one-dimensional system: the channel waveguide in a two-dimensional photonic crystal," Phys. Rev. B **63**(11), 113311 (2001).
16. H. Benisty, N. Piskunov, P. N. Kashkarov, and O. Khayam, "Crossing of manifolds leads to flat dispersion: Blazed Littrow waveguides," Phys. Rev. A **84**(6), 063825 (2011).
17. O. Khayam and H. Benisty, "General recipe for flatbands in photonic crystal waveguides," Opt. Express **17**(17), 14634–14648 (2009).
18. D. Rosenblatt, A. Sharon, and A. A. Friesem, "Resonant Grating Waveguide Structures," IEEE J. Quantum Electron. **33**(11), 2038–2059 (1997).
19. A. David, H. Benisty, and C. Weisbuch, "Photonic crystal light-emitting sources," Rep. Prog. Phys. **75**(12), 126501 (2012).

1. Introduction

The interest of hybrid silicon photonics, with III-V active material bonded onto a platform such as Silicon-On-Insulator (SOI), is undisputed [1–3]. One first point was to get guidance from well mastered low-loss silicon structures, and to get active emission from the III-V epitaxial heterostructure stack (denoted EHS below), either in combination or for separate action, with a transfer in between. For these optical functions, bonding can make use of oxide, or polymer (e.g., benzocyclobutene BCB). Attempts have been pursued for bonding layer down to a few nm or of molecular nature [4]. GaAs-Si bonding without oxide is also sought actively [5,6] for the useful 1300 nm emission. Oxide-free bonding [7], is the only known technique to date that ensures not only a mechanical and thermal bond, but also an electrical bond, i.e. a low impedance non rectifying contact between silicon and EHS, as shown recently [8] for InP-Si bonding (Refs [5,6] show a non-rectifying Si-GaAs contact). Echoing the numerous novel uses of subwavelength structures in silicon photonics [9], oxide-free bonding of *nanostructured* silicon to III-V EHS was also demonstrated successfully [10], with positive photonics tests [11]. Besides a possible ohmic use, nanopatterns offer the capability of lateral guidance combined with additionally lateral thermal sinking in the upper silicon slab [12].

In this work, we argue that when an electrical contact across the bonded Si/EHS interface is desired, the natural vertical modal engineering practiced with the oxide (SiO_2) or polymer barrier is absent. Then, the stack's fundamental mode (FM) may widely overlap the Si slab, hence a penalty for a laser structure, as the confinement factor Γ_{FM} of the active quantum wells (QWs) is reduced. To circumvent this penalty, we show that a nanopatterned silicon consisting of an array of holes with a modest air fraction f acts as a low-index barrier between Si and EHS, and thus greatly assists laser operation in the established regime of III-V's Separate Confinement Heterostructures (SCH). To evidence this, we analyze the dispersion of the Si-EHS stack: we excite guided modes by the localized QWs photoluminescence and out-couple them thanks to a superperiodic modulation of the basic sub-wavelength nanopattern. We first detail the sample, the experiment, and illustrate the TE polarized mode distribution undergoing confinement by the low-index barrier. We finally present the main experimental results.

2. Sample and experimental set-up

We show a schematic cross-section of our stack in Fig. 1(a) [7]. The silicon slab of the SOI is 500-nm-thick, the EHS has a 380-nm-thick SCH with QWs emitting at 1505 nm, sandwiched

between 100 nm InP on the Si side, and 820 nm InP on the top (air) side to avoid that the FM visits the top surface. A representative cross-section of an oxide-free bonded SOI-EHS with nanopatterned silicon (here about 200nm) and QW revelation is shown in Fig. 1(b). In our photonic study, the etch-depth is 270 nm, leaving 230 nm un-etched Si.

In Fig. 1(c), we sketch an injected laser diode exploiting silicon to spread the current below the QWs, thus reducing Joule heating near the active junction. High doping is then needed in silicon. Without nanopattern, this doping would cause residual absorption in Si as the FM would overlap this region (usually a TE mode, fitted to exploit e-hh transitions in QWs). It is therefore welcome to repel the FM profile up into the EHS, a feature that, in addition, increases Γ_{FM} for this mode. The nanopattern lowers the Si index ~3.48 to an homogenized in-plane effective index $n_{hom,xy}$ ~2.8-3.3, well suited for this purpose. We will denote $n_{eff,z}$ the effective indices of guided modes (pertaining to index profile in the z-direction).

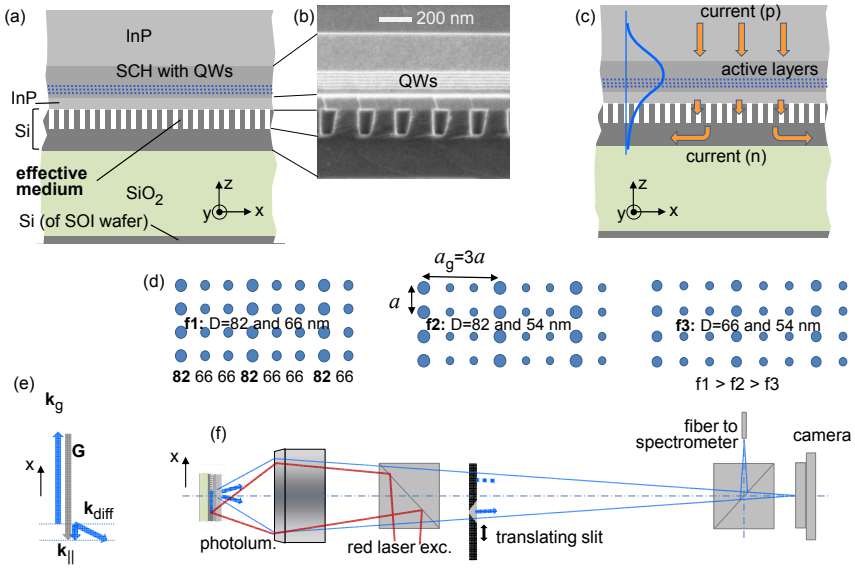

Fig. 1. (a) Effective medium made of nanostructured silicon in a hybrid silicon-III-V heterostructure elaborated by oxide-free bonding; (b) Micrograph of the slab section with quantum-wells revealed; (c) scheme of electrical injection and fundamental mode profile allowed by the lowered index of nanostructured silicon; (d) Modulated square lattices with every third hole slightly bigger with the three pairs of diameters used; (e) Ewald diagram for diffraction in air; (f) set-up to get an angular spectrum by translating a slit in the imaging path.

The chosen nanopattern is a square array of holes. For the sole use as a low-index layer, any sub-wavelength period $a < \lambda/2n_{eff,z}$ ~215 nm suffices, but no easy diagnostic of its photonic role at device scale (say > 50 µm) can be made [11]. We therefore add a weak one-dimensional periodicity along x, by enlarging every third hole. As shown in Fig. 1(d), there are three hole diameters used in three pair combinations, lithography and etching technologies being optimized to deliver vertical walls. The result is a set of three designs, labelled $f_1(82,66)$, $f_2(82,54)$ and $f_3(66,54)$, (d_i,D_i) being the two diameters in nm, with decreasing air fractions f_i (thus, increasing $n_{eff,xy}$). These modulated patterns are essentially equivalent to a superposition of (i) arrays of uniform diameters 72 nm, 65 nm, 58 nm for f_1, f_2, f_3 respectively (based on the same average hole area, e.g. $72^2 \approx [82^2 + 66^2 + 66^2]/3$) with (ii) a $3a$-period modulation. The diffraction efficiency of this modulation is given by the relevant Fourier component A_G of the xy dielectric map at wavevector $G = G_x = 2\pi/3a$ along x (actually not needed here).

Typically, we operate to extract modes of indices 3.0-3.2 at λ = 1500 nm around normal incidence, hence $3a$ ~480 nm. The air-filling factors are then $f_1 = 0.158$, $f_2 = 0.128$, $f_3 = 0.104$. Applied to a uniform medium of index 3.48 (Si) with infinite air cylinders in the microscopic limit ($d << \lambda$), they have homogenized indices $n_{hom,xy}$ of about 3.04, 3.13 and 3.19, calculated from a standard two-dimensional plane-wave expansion. We note that ellipsometry could seem a suitable technique for establishing the index sequence, but for transparent substrates, thick top layers, small patterns (~50 μm) and small InP bonded pieces (large sizes are not routine yet), it seems too awkward. In Fig. 1(e,f) the setup used for measurement is explained. It resembles that of [13] used for guided mode extraction studies. A red laser excites a photoluminescent spot inducing radially expanding guided waves. Those waves launched along x meet the effective medium (70 × 30 μm patches) in which the nanopattern modulation causes diffraction and outcoupling. Behind the objective and the beam splitter, a slit is translated to select the beam waves with a given in-plane direction $k_{||} \equiv k_x$ according to the Ewald construction of Fig. 1(e), $k_{||} = k_g - G$, $k_g = n_{eff,z}\, k_o$ being a guided mode wavevector, and denoting $k_o = 2\pi/\lambda$. A second splitter provides imaging with an infrared camera as well as a fibered path to a spectrometer equipped with an InGaAs cooled array.

3. Dispersion analysis

We first calculated the several TE and TM guided modes of the SOI + EHS stack using tabulated Si, SiO_2 and InP dispersion laws $n(\lambda)$ without absorption. In Fig. 2(a), we vary $n_{hom,xy}$ ("effective medium", Fig. 2(b)) and plot all branches at a fixed wavelength λ = 1505 nm. We replaced the whole SCH by a single 380 nm-thick purely dispersive layer with typical Sellmeier parameters [14], Fig. 2(c), chosen to fit experimental data for all modes of the stack.

The most salient feature around our range, $n_{hom,xy}$ ~3.0, is the TE1/TE2 anticrossing. The presence of such an anticrossing is typical of a mode residing or not on one side of the low index barrier upon interaction with the mode on the other side. As for the fundamental mode, there is a broad smeared anticrossing immediately at $n_{hom,xy}$ ~3.4, which is indicative of the Si attraction for the mode when it is pure. We hope to mitigate this feature thanks to the low index effective medium (it would be less smeared with a first InP layer of >100 nm). Nevertheless, assessing the small shifts of $n_{eff,z}$ for TE0 with our set-up is not very reliable. Instead the TE1/TE2 anticrossing offers a remarkable signature of the role of $n_{hom,xy}$.

To understand more explicitly the role of the low-index barrier, we plot on Fig. 2(d-g) the modal profiles of the three first TE modes for illustrative situations close to the four actual cases: no holes, f_3, f_2, f_1. In this order the index $n_{hom,xy}$ decreases. We push the lower bound to 2.93, instead of the actual one (~3.00) to better visualize the fate of higher modes.

We first see that for pure silicon, the FM mostly lies within the silicon layer. This pertains also to the choice of a rather thick silicon slab (500 nm). It is a good typical value, and could be useful, either to carry intense current, or to sink substantial heat sideways off a structure's active junction. But we also see that as soon as air is introduced, for the f_3 sample and $n_{hom,xy}$~3.23, the FM is clearly centered in the SCH, and its overlap with the nanopattern is quite low. As more air is introduced, going from f_3 to f_2 and to f_1, the overlap of the SCH guided mode with the pattern still diminishes, and all parts of the mode profile are pushed toward the SCH.

The origin of the anticrossing of modes TE1 and TE2 can also be inferred from the profiles: for f_3, TE1 occupies the silicon and TE2 lies rather in the III-V stack (the EHS), whereas for f_1, we observe almost the contrary: TE2 now manages to be in the silicon region, while TE1 has a substantial lobe in the EHS. These considerations will be useful to explain experimental data that will be presented in the following section.

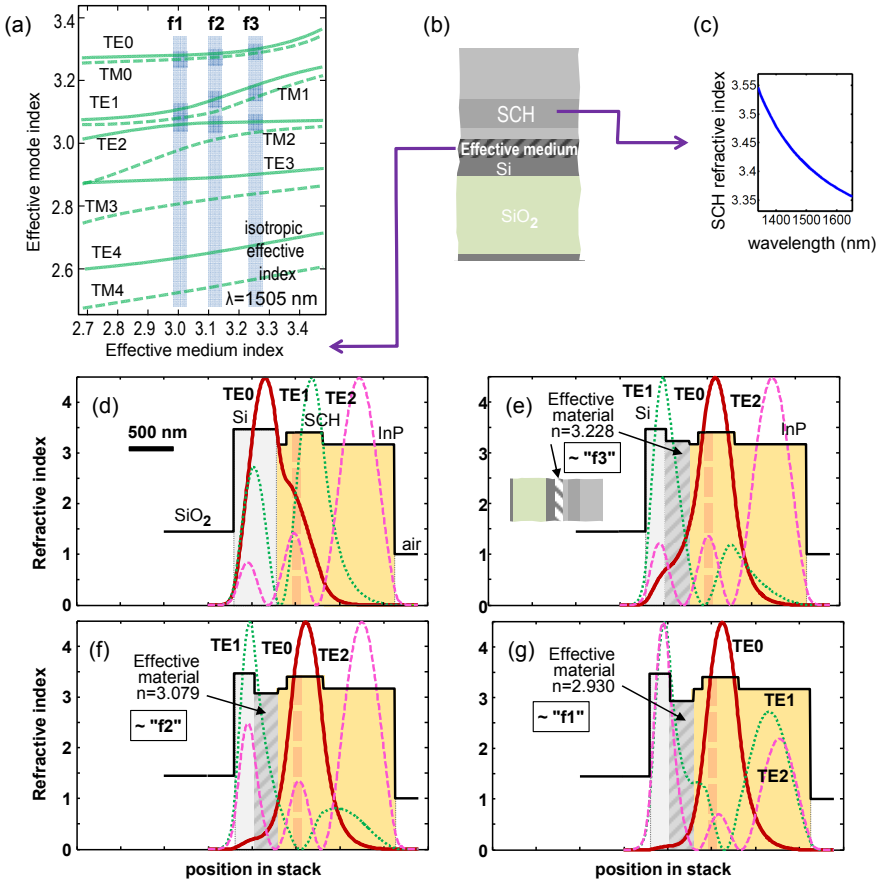

Fig. 2. (a) Expected effective indices of TE and TM modes for the simplified heterostructure as a function of an isotropic effective-material low index slab of 270 nm replacing the silicon top part. Note the anticrossing behavior of the TE1 and TE2 modes around an effective-material index n~3; (b) Structure stack; (c) Average index of a typical SCH layer; (d) Mode profiles of the first three TE modes in the non-etched bonded stack at λ = 1505 nm; (e) Same with a nanostructured layer of ~isotropic index $n_{hom,xy} = n_{Si} - 0.25$~3.23; (f) Same with $n_{hom,xy} = n_{Si} - 0.40$ ~3.08; (g) Same with $n_{hom,xy} = n_{Si} - 0.55$ ~2.93. The fundamental mode is repelled in the III-V stack for lower $n_{hom,xy}$. Its overlap with the nanostructured layer decreases. The anticrossing behavior of modes TE1 and TE2 clearly appears as Si guidance is driven to lower effective indices by the diminishing $n_{hom,xy}$.

4. Dispersion characterization and discussion

The experimental angular resolved spectra shown below are obtained with a ~350 µm slit scanned on ~8 mm across the beam behind the objective whose limits are $k_{||}/k_o \approx \pm 0.40$ (NA).

These angular spectra are represented as color maps in Fig. 3(a-c) for a = 160 nm and Fig. 3(d-f) for a = 170 nm. There is a rich content, with lines of quite modulated intensity and some quite visible gaps: in Brillouin zone center $k_{||}/k_o = 0$ for forward/backward coupling of the same mode, or at other positions if distinct modes are interacting. This is as expected from a broad periodic multimode guide [15–18]. However, our concern is simply the modal sequence of underlying unperturbed modes (smooth branches without their gaps) to evidence the role of $n_{hom,xy}$ according to the above analysis. We are of course aware that gaps and signal strength reveal the degree of interaction of the mode with the lattice, further mitigated by various interference effects [19]. Hence, to fit our modeling, we first adjusted thicknesses and angle calibration from all measured samples (dots on Fig. 3(a-f), TE in dark blue, TM in

green), which includes some other periods not shown here, taking notably high order modes ($n_{eff,z}$<2) into account. This adjustment consolidated the above mentioned thicknesses and SCH dispersion function of Fig. 2 (c). We adjusted in this process the value of $n_{hom,xy}$ to reproduce in particular the first three modes of the sequence, which, with our resolution and diffraction geometry, amount to TE0, TE1, TE2 (marked with bluish half-transparent ribbons in Fig. 3).

The indices that we found correspond to the grey bands of Fig. 2(a), whose width accounts for the slight data scatter ($\Delta n \sim 0.03$). Relatively accurate values of effective indices $n_{eff,z}$ were deduced from the spectra. Since they were found to fit with the expectations (see the dotted fits on all spectra maps), it also means that the absolute values for *all* branches in Fig. 2(a) along the vertical grey bands are the actual ones for this oxide-free bonded sample, helping to clarify other future investigations. Values of $n_{hom,xy}$ are somewhat more spread than predicted by the hole-diameter-based prediction, spanning [3.00 → 3.25] instead of [3.04 → 3.19]. We see that the three first modes' unmistakable evolution along the sequence $f_1 \rightarrow f_2 \rightarrow f_3$ [darker shades in grey bands, Fig. 2(a)], is well reproduced experimentally in the observed branch spacing. Note the weakness of the TE0 line through all data. It reflects the weak profile amplitude at the grating locus, showing that this mode is rather centered on the SCH, as noted in the above analysis. But the diffracted intensity cannot be naively used as a probe of that interaction because it involves also the quite variable reflection of bottom-diffracted waves onto the SOI stack [10].

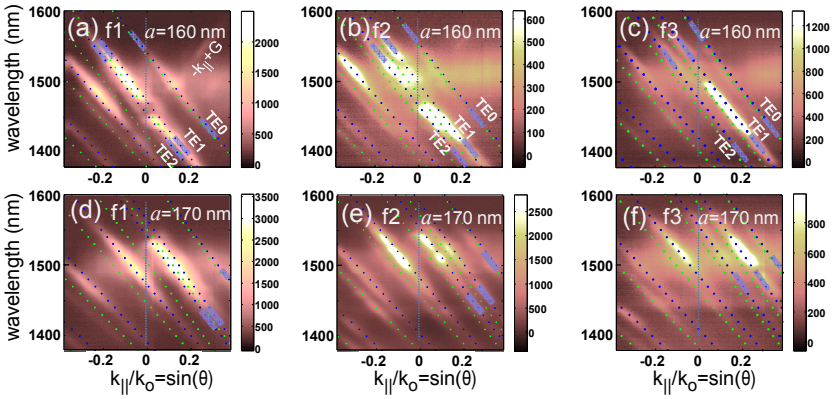

Fig. 3. (a-c) Experimental angular spectra (abscissa: $k_{//}/k_o \equiv$ numerical aperture) for the three filling factors (f_1, f_2, f_3) and for the period 480nm = 3 × 160 nm; (d-f) Same for the period 510 nm = 3 × 170 nm; calculated TE branches are the blue dots, TM ones are the green dots. Bluish semi-transparent rectangles at top and bottom of maps underline modes TE0, TE1, TE2.

5. Conclusion

We have evidenced the positive role of a nanopatterned silicon acting as an effective low-index layer for the good operation of active optoelectronics of a III-V stack in the new silicon photonics configuration permitted by oxide-free void-free bonding: Electrical contact seems effective in this geometry [8], but the possible penalty of excessively attracting the useful (lasing) mode away from the active SCH into the silicon has to be mitigated. We have evidenced that a nanopatterned silicon layer of typical thickness 250-300 nm, air fraction f = 0.1-0.2, with a square lattice period 150-180 nm could work well in this respect. The hole diameters involved, about 55-85 nm, are well suited to state-of-the-art technology, making this approach helpful for forthcoming silicon photonic devices.

Acknowledgments

We acknowledge the support of French ANR through the COHEDIO project.